applied sciences

MDPI

Article

Digital Core Analysis on Water Sensitivity Mechanism and Pore Structure Evolution of Low-Clay Tight Conglomerate

Dunqing Liu [1,*], Keji Chen [1] and Erhan Shi [2]

[1] Faculty of Petroleum, China University of Petroleum (Beijing) at Karamay, Karamay 834000, China
[2] Exploration and Development Research Institute, PetroChina Southwest Oil & Gas Field Company, Chengdu 610041, China; shierhansw@petrochina.com.cn
* Correspondence: liudunqing@cupk.edu.cn

Abstract

This study investigates the mechanisms behind strong water sensitivity in some low-clay-mineral-content tight conglomerate reservoirs in China's Mahu Sag. Using core-scale water sensitivity tests, mineral analysis, in situ micro-CT scanning, and digital core techniques, we analyzed how water sensitivity alters pore structures across cores of varying permeability. Key findings include the following: (1) Water sensitivity damage increases as initial gas permeability decreases. (2) Despite low clay content, significant water sensitivity arises from the combined effect of water and velocity sensitivity, driven mainly by illite and kaolinite concentrated in gravel-edge fractures and key flow channels. (3) Water sensitivity causes non-uniform pore structure changes—some macropores and throats enlarge locally, reflecting heterogeneity. (4) Structural responses differ by permeability: medium–low permeability cores suffer from clay mineral swelling and particle migration, whereas high-permeability cores resist overall damage and may even have main flow paths enhanced by flushing. (5) Water sensitivity mainly degrades smaller pores but can improve larger ones, with the critical pore-size threshold between macro- and micro-pores inversely related to permeability. This work clarifies the pore-scale mechanisms of water sensitivity in some low-clay-mineral-content tight conglomerates, and can provide guidance for the optimization of water types injected into similar conglomerate reservoirs.

Keywords: tight conglomerates; micro-CT; water sensitivity; digital core

check for updates

Academic Editor: Tiago Filipe da Silva Miranda

Received: 19 October 2025
Revised: 11 November 2025
Accepted: 12 November 2025
Published: 15 November 2025

Citation: Liu, D.; Chen, K.; Shi, E. Digital Core Analysis on Water Sensitivity Mechanism and Pore Structure Evolution of Low-Clay Tight Conglomerate. *Appl. Sci.* **2025**, *15*, 12136. https://doi.org/10.3390/app152212136

Copyright: © 2025 by the authors. Licensee MDPI, Basel, Switzerland. This article is an open access article distributed under the terms and conditions of the Creative Commons Attribution (CC BY) license (https://creativecommons.org/licenses/by/4.0/).

1. Introduction

Conglomerate reservoirs in the Junggar Basin, Xinjiang, China, have garnered significant attention in recent years, particularly following the discovery of billion-ton oil and gas resources in 2014 [1–3]. These reservoirs are generally characterized by weak natural energy or low permeability, necessitating external fluid injection for energy supplement or fracture stimulation to maintain production during later development stages. Compared to conventional or tight sandstone reservoirs, conglomerates consist of gravels of varying sizes and finer detrital matrix, resulting in complex pore structures, diverse mineral composition, and pronounced heterogeneity [4,5]. Furthermore, the permeability of these reservoirs demonstrates heightened sensitivity to stress and foreign fluids, significantly impeding the efficient development of their hydrocarbon resources [6–8].

Water sensitivity damage is a major cause of permeability impairment in conglomerate reservoirs. Conventional understanding attributes this damage primarily to the swelling and dispersion of clay minerals upon contact with aqueous fluids, with the degree of

sensitivity strongly correlated to total and specific clay mineral content [9]. Consequently, clay mineral content and type are often used in the field to assess permeability sensitivity risk and to guide the optimization of injection water sources [10]. While this empirical approach demonstrates applicability in many reservoir formations, it presents unexpected limitations when applied to specific tight conglomerate reservoirs.

Unlike the extensively studied tight sandstone and shale reservoirs, conglomerates feature a tripartite structure of gravel, matrix, and cement. Their pore systems are complex and highly heterogeneous, including gravel-edge fractures, trans-gravel fractures, inner-gravel dissolution pores, intergranular pores, micro-fractures, and dissolution pores in inter-gravel matrix [11,12]. Additionally, the composition of gravels themselves varies widely, and the types of inter-gravel matrix and cement are diverse. These factors lead to significant variations in clay mineral type, content, and spatial distribution, weakening the correlation between bulk clay mineral content and permeability sensitivity observed in practice [5,13].

Taking the conglomerate reservoir in this study as an example, during its mid-to-late development stages, reservoir energy depletion led to severe production decline. To enhance output, water flooding was implemented. In optimizing the water source, core analysis revealed a total clay mineral content of less than 5%. Consequently, no specific water sensitivity control measures were applied to the injected water. In previous studies, the critical clay mineral content that can cause serious water sensitivity in these conglomerate reservoirs is generally considered to exceed 16% [14]. However, field observations indicate noticeable water sensitivity phenomena even in sections with low clay mineral content, manifesting as difficulties in fluid injection, significant permeability reduction, and rapid production decline. Moreover, the pore sizes and permeability ranges in conglomerate reservoirs span widely. Within the same production interval, layers of different sizes and permeabilities are affected dissimilarly by water sensitivity, leading to scenarios where some perforation clusters experience injection difficulties while others remain unaffected. The field is currently hindered by an unclear understanding of both the formation mechanism of strong water sensitivity and its varying degrees across intervals. Consequently, injection fluid optimization lacks an empirical basis, compounding both the risks and the marginal costs of water injection operations. Consequently, it is imperative for the field to conduct dedicated research to gain a clear understanding of this matter.

In recent years, the evaluation and development of conglomerate reservoirs in China have become increasingly refined, with analyses of reservoir sensitivity, movable oil, and residual oil distribution advancing to the pore scale [15–17]. The current standard method for evaluating permeability sensitivity (damage degree) relies on core flow tests, which involve multiple fluid cycles, extended durations, complex procedures, and crucially, lack the capability for quantitative analysis of specific pore structural variations, thus failing to meet the demands of pore-scale sensitivity assessment. Micro-CT is a widely adopted and mature technique for analyzing material microstructures. Combining micro-CT with digital rock image analysis enables the quantitative characterization of parameters such as pore size, throat size, connectivity, and coordination number in core samples [18]. The development of in situ CT technology further allows for the quantitative analysis of in situ changes in pore structure under varying conditions. This approach has been successfully applied to visualize fracture evolution in cores, observe and quantify high-temperature damage processes in composites, and characterize the evolution of pore and permeability parameters in cores under different temperatures and pressures [19]. Given that permeability damage before and after water flooding fundamentally stems from alterations in the internal pore structure, the quantitative evaluation of pore structure changes due to water sensitivity can also be effectively achieved through in situ micro-CT.

Addressing the need for more quantitative sensitivity analysis in conglomerates and elucidating the mechanisms behind strong water sensitivity in some Mahu Sag conglomerate reservoirs with low clay mineral content. Bottom hole cores were collected, and we conducted water sensitivity evaluations, and XRD and RoqSCAN technologies were employed to determine the mineral composition and distribution of the cores. Furthermore, CT was used to acquire pore structure parameters of the samples before and after water sensitivity damage. Through these experiments, the relationship between the degree of water sensitivity and permeability for the conglomerate cores was established, the formation mechanism of water sensitivity under low clay mineral content was revealed, and the changes in pore structure parameters before and after water sensitivity of samples with different permeability ranges were quantitatively characterized. This research contributes to a deeper understanding of water sensitivity mechanisms in the Mahu Sag conglomerates and provides a quantitative analysis of the impact of water sensitivity on pore structure parameters. These findings provide valuable guidance for optimizing fluid injection designs in the field.

2. Samples and Methods

2.1. Water Sensitivity Evaluation

Several conglomerate plug samples were drilled using kerosene from two exploration wells in Xinjiang Oilfield. Most plugs had a diameter of 1 inch, with a minority at 1.5 inches. The drilled plugs were trimmed using a water-free wire saw to achieve flat end faces. Subsequently, the trimmed plugs were subjected to a two-week oil extraction process using organic solvents, followed by solvent removal in a vacuum drying oven. The dimensions of the dried core samples were measured using a digital vernier caliper. Gas permeability was determined by the steady-state method using high-purity nitrogen (99.9 wt.%). The confining pressure was set at 1.5 MPa, and the pore pressure was maintained below 0.6 MPa. The gas flow rate was measured using a photoelectric flow meter after the outlet gas flow stabilized. Based on the permeability range, seven samples with varied permeability were selected for water sensitivity analysis. The porosity of these seven samples was determined from their dry weight, the wet weight after saturation with formation water during the water sensitivity analysis stage, the density of the saturated formation fluid, and their dimensions. The basic parameters of the samples used for water sensitivity analysis are presented in Table 1.

Table 1. Basic information about the samples.

Core NO.	Length/cm	Width/cm	Porosity/%	Gas Permeability/μm^2
A1	6.30	2.44	9.92	0.74
A2	6.73	2.46	6.98	0.80
A3	7.46	2.46	10.27	3.81
A4	6.86	2.45	10.28	5.12
A5	5.91	3.83	7.57	2.13
A6	3.15	2.47	9.66	19.74
A7	5.32	2.46	8.13	50.63

The procedure for the water sensitivity test refers to the industry standard SY/T 5358-2010: evaluation methods for reservoir sensitivity flow experiments [20]. Prior to the test, simulated formation water was prepared based on formation water information, with the specific composition detailed in Table 2.

Table 2. Mineral composition of the formation water.

Ion Type	CO_3^{2-}	HCO_3^{2-}	SO_4^{2-}	Cl^-	Ca^{2-}	Mg^{2-}	$K^+ + Na^+$
Concentration/mg·L^{-1}	180.63	1592.01	110.71	21,253.5	138.87	43.5	14,338.89

In the water sensitivity test, simulated formation water was initially injected at a constant rate of 0.5 mL/min for 15 to 20 pore volumes (PV). The baseline permeability (K_b) was calculated based on the inlet pressure and dimensional parameters of the sample. The fluid was then switched to simulated formation water with half of the original concentration, and injection continued at the same rate for 15 to 20 PV. Finally, distilled water was injected under the same constant flow rate conditions, during which the permeability (K_w) was measured. The damage rate (D_w) of the sample was calculated using Equation (1).

$$D_w = \frac{|K_b - K_w|}{K_b} \times 100\% \quad (1)$$

2.2. Mineral Composition

The mineral composition of the core samples was determined using both XRD and RoqSCAN techniques, and the samples were remnants from trimming the plug ends. Samples for XRD analysis were crushed to approximately 200 mesh. A SmartLab X-ray diffractometer was used, following the standard SY/T 5163-2018: Analysis of clay minerals and common non-clay minerals in sedimentary rocks by X-ray diffraction [21], to obtain the mineral compositions and contents. Samples for RoqSCAN analysis were obtained from remnants of four plugs with varying permeabilities. They were prepared into flake samples approximately 4 mm thick and 1.5 cm^2 in area using wire cutting, followed by mechanical polishing and argon ion polishing, and finally coated with a carbon film. The RoqSCAN technology was then used to scan the mineral composition on the sample surface with a step size of 50 μm. The sample IDs and corresponding permeabilities of the four plugs are: B1–4.01 mD, B2–1.78 mD, B3–0.57 mD, B4–0.82 mD.

2.3. CT Scanning and Data Analysis

Based on the gas permeability results, three plugs representing different permeability levels were selected: 1.96 mD (Sample C1), 11.22 mD (Sample C2), and 59.5 mD (Sample C3). Small plugs with a diameter of 5 mm were cut from the 1-inch plugs using water-free wire cutting. Subsequently, sections approximately 1.5 cm in length with flat surfaces were cut from the intact small plugs and wrapped with heat-shrink tubing (as shown in Figure 1). The small plugs were then placed into a carbon fiber core holder. A confining pressure of 1.2 MPa was applied. Formation water was injected at a rate of 0.02 mL/min until the cumulative water production at the outlet reached about 2 mL. After aging for 12 h, a region approximately 5 mm in the middle of the small plug sample was scanned. After the scan, distilled water was injected at the same rate until the cumulative water production reached about 2 mL, followed by another 12 h aging period. The same position was scanned again with identical parameters. The micro-CT used was nanoVoxel-4000, with scanning parameters set at 160 kV and 60 μA. Image data were exported as a 16-bit grayscale RAW file with a voxel resolution of 1.89 μm.

Image files were further processed using PerGeos 2020.1 software. The hardware platform for data processing was equipped with an AMD EPYC 9654 processor (96 cores, 3.7 GHz), 768 GB of RAM (4800 MHz), and an NVIDIA RTX 4090 graphics card (24 GB VRAM). After loading the data, the grayscale was normalized to [0–65,535] to ensure a unified grayscale range for the datasets scanned before and after water flooding. A unified grayscale range facilitates consistent threshold selection for subsequent pore

segmentation, reducing pore identification errors caused by threshold variations. Median filtering was then applied to denoise and smooth the images. After filtering, sub-volumes were extracted from regions rich in pores. The scale of the sub-volume region was about 1300 × 1300 × 700 voxels. Interactive threshold segmentation was performed on the sub-volume, and the top-hat method was used to enhance the identification of micro-fractures. The segmented pore regions were analyzed using label analysis to separate individual pores, followed by the extraction of a pore network model (PNM). Finally, parameters related to the pore network were calculated based on the PNM.

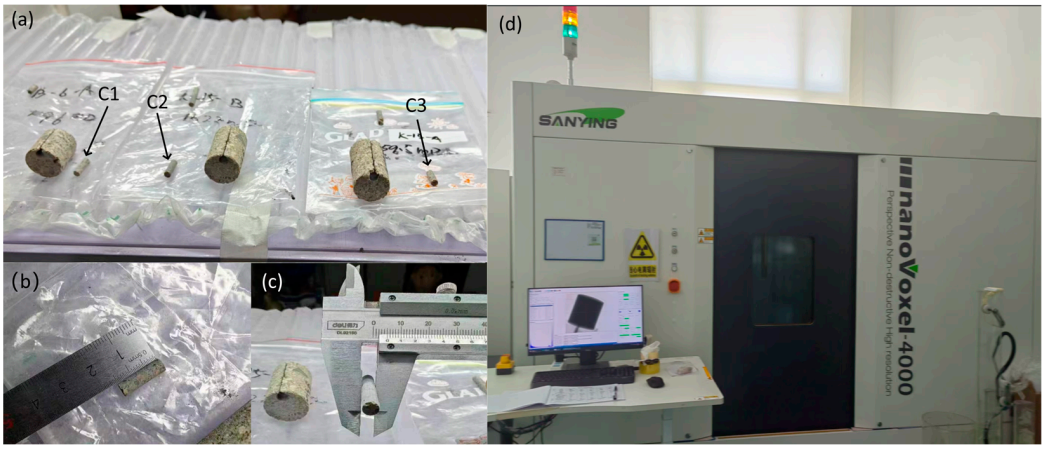


Figure 1. Samples for micro-CT scan. (**a**) The 1-inch plugs and the corresponding 5mm small plugs. (**b**,**c**) The size of the small plug. (**d**) The micro-CT used in this study.

3. Results

3.1. Water Sensitivity Results

The gas permeability of the seven samples ranged from 0.74 mD to 50.63 mD, comprising two samples below 1 mD, three samples between 1 mD and 10 mD, and two samples above 10 mD. The specific water sensitivity coefficients are provided in Table 3, with the corresponding water sensitivity degrees classified according to the industry standard SY/T 5358-2010 [20]. Except for the sample with a gas permeability of 50.63 mD, the remaining six samples exhibited varying degrees of water sensitivity damage. Sample A1, with a gas permeability of 0.74 mD, showed extremely strong water sensitivity, exhibiting a permeability reduction of 93.14%. Another sample, A2, with a gas permeability of 0.8 mD, had a permeability loss rate of 82.57% after distilled water flooding, also categorized as strong water sensitivity. Among the three samples with permeabilities between 1 mD and 10 mD, sample A4 (5.12 mD) showed a permeability loss rate of 69.07%, classified as moderately strong. The other two samples, A5 (2.13 mD) and A3 (3.81 mD), exhibited permeability reductions of 78.04% and 75.29%, respectively, after distilled water flooding, also indicating strong water sensitivity. Finally, the two samples with permeabilities above 10 mD fell into the medium and weak water sensitivity ranges, respectively.

The permeability loss rate of the samples in the study area showed an inverse correlation with the gas permeability, as shown in Figure 2.

The correlation coefficient for the linear fitting relationship between the gas permeability (logarithmic axis) and the permeability loss rate in the water sensitivity test for the seven samples reached 0.94. Based on the intersection points between the fitted relationship curve and the existing water sensitivity classification standard boundaries, the approximate gas permeability boundaries for cores with different water sensitivity degrees in this study area can be determined. It can be seen that the gas permeability boundary for strong water sensitivity in the cores of this study area is approximately 3 mD, and permeability below

0.7 mD reaches the extremely strong water sensitivity range. The gas permeability range for medium water sensitivity is relatively wide, from 3 mD to 67 mD, with 14 mD as the boundary between moderately strong and moderately weak. These boundaries can be used to quickly assess the degree and range of water sensitivity in the reservoirs of the study area.

Table 3. Water sensitivity results of the plug samples.

Cores	Porosity/%	Gas Permeability/μm^2	Formation Water Permeability/μm^2	Distilled Water Permeability/μm^2	Permeability Loss Rate/%	Water Sensitivity Degree
A1	9.92	0.74	0.19	0.01	93.14	Very Strong
A2	6.98	0.8	0.29	0.05	82.57	strong
A3	10.27	3.81	0.91	0.22	75.29	strong
A4	10.28	5.12	1.92	0.61	69.07	moderately strong
A5	7.57	2.13	0.89	0.2	78.04	strong
A6	9.66	19.74	11.56	5.52	52.25	medium
A7	8.13	50.63	39.63	30.04	24.19	weak

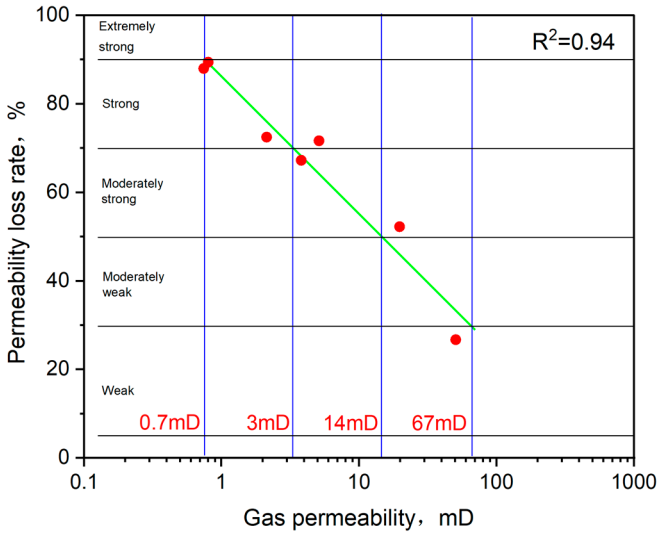


Figure 2. Relationship between gas permeability and permeability loss rate in the water sensitivity test. The red dots are the permeability loss rate of the samples and the green line represents the linear fitting trend line.

3.2. Mineral Composition Results

Clay minerals are an important factor in inducing water sensitivity. The XRD analysis results of the samples used for sensitivity analysis are shown in Table 4, and the corresponding clay mineral types and contents are shown in Table 5.

Table 4. Mineralogical composition of the water sensitivity test cores.

Cores	XRD Mineralogical Composition (wt.%)					
	Quartz	K-Feldspar	Plagioclase	Calcite	Dolomite	Clay
A1	21.6	21.9	46.9	4.2	1.2	4.2
A2	27.3	19.2	38.7	11.5	0.8	2.5
A3	33.2	17.1	37	10.3	0.6	1.8
A4	21.3	16.3	50.3	8.2	0.8	3.1
A5	24.7	28.2	43	0	0.9	3.2
A6	18.8	9.3	57.7	9.4	0	4.8
A7	20.7	14.6	59.5	0	0.7	4.5

Table 5. Clay mineralogical composition of the water sensitivity test cores.

Cores	XRD Clay Mineralogical Composition (wt.%)					I/S Ratio (%)	
	S	I	K	C	I/S	S %	I %
A1	0	19	48	9	24	20	80
A2	0	19	53	0	28	20	80
A3	0	14	44	15	27	20	80
A4	0	18	45	12	25	20	80
A5	0	14	60	0	26	20	80
A6	0	9	57	20	14	20	80
A7	0	7	43	38	12	20	80

S: smectite; I: illite; K: kaolinite; C: chlorite; I/S: illite-smectite interlayer.

The clay mineral content of all seven samples was below 5%. Plagioclase was the most abundant mineral, followed by quartz and K-feldspar. Calcite and dolomite showed the lowest proportions; calcite was not detected in two samples, with an average content of approximately 8.7%, while the dolomite content was generally below 1%. Among the clay minerals, kaolinite was the most prevalent, averaging about 50%, followed by illite–smectite mixed-layer minerals at around 22.3%, and finally illite and chlorite, with average contents of 14.3% and 13.4%, respectively.

The results indicate that the total clay mineral content in the core samples is less than 5%, and the dominant clay mineral is not montmorillonite, which has the highest swelling potential. Instead, the most abundant clay is kaolinite, a velocity-sensitive mineral. Illite exhibits both velocity sensitivity and moderate swelling capacity, while chlorite is an acid-sensitive mineral. Such low clay mineral content in sandstone reservoirs would typically suggest a lower risk of water sensitivity. However, in the conglomerates of this study area, significant and widespread water sensitivity was still observed. This implies that the threshold clay mineral content required to trigger water sensitivity in conglomerate reservoirs may be considerably lower than that in tight sandstones.

The gas permeabilities of the plugs corresponding to the RoqSCAN analyzed samples were 0.57 mD, 0.82 mD, 1.78 mD, and 4.01 mD, respectively. According to the relationship chart between gas permeability and water sensitivity from the previous section, these four samples all fall within the strong water sensitivity range. The mineral and clay mineral contents obtained from RoqSCAN are shown in Tables 6 and 7. The mineral components were roughly categorized into total siliceous minerals, total calcium minerals, total clay minerals, and other minerals. It can be seen that the results obtained by RoqSCAN are very close to the XRD results. Siliceous minerals account for over 80% of the mineral composition, followed by calcium minerals. Clay minerals account for less than 5%, and other minerals account for an average of less than 5%.

Table 6. Mineralogical composition of the RoqSCAN cores.

Cores	RoqSCAN Mineralogical Composition/wt.%			
	Total Siliceous Minerals	Total Calcium Minerals	Total Clay Minerals	Total Other Minerals
B1	86.92	7.79	2.23	3.08
B2	90.14	0	2.92	6.92
B3	89.13	0.46	3.07	7.29
B4	84.82	10.81	1.91	2.45

Table 7. Clay mineralogical composition of the RoqSCAN cores.

Cores	RoqSCAN Clay Mineralogical Composition/wt.%				
	Mica	**Kaolinite**	**Chlorite**	**Illite**	**Illite/Smectite**
B1	17.93	21.97	7.17	48.43	4.48
B2	7.19	6.51	23.29	54.79	8.22
B3	12.05	23.45	6.51	57.33	0.65
B4	14.66	13.09	9.42	60.73	2.09

The surface mineral composition distribution results obtained by RoqSCAN are shown in Figures 3 and 4. The surface morphology and mineral distribution of the samples partly explain the formation mechanism of strong water sensitivity under low total clay mineral content in the study area.

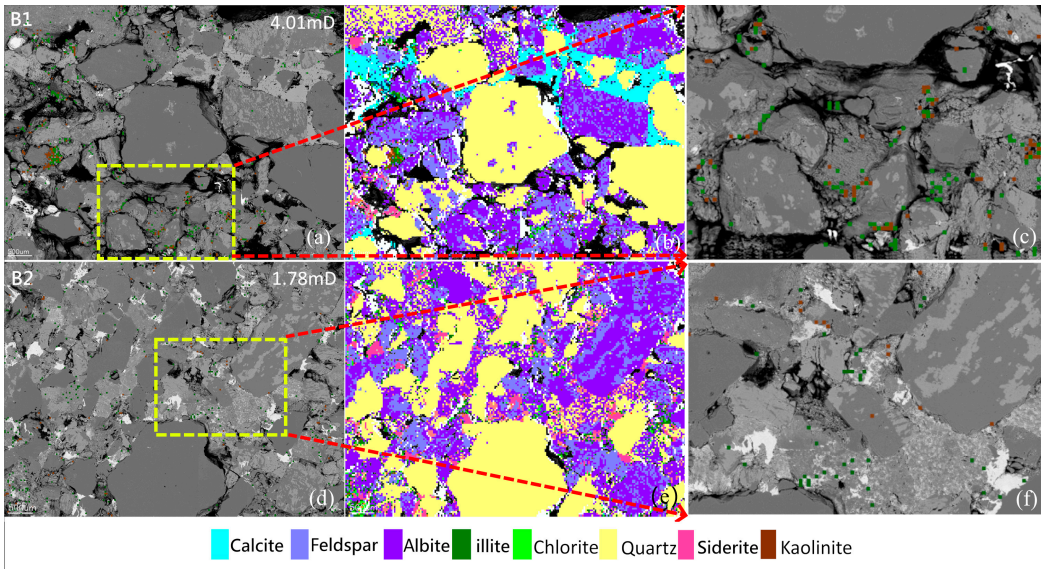


Figure 3. Surface morphology and mineral composition distribution of samples B1 and B2. (**a**) SEM image of sample B1 overlaid with illite and kaolinite distribution, (**b**) overall mineral composition distribution of sample B1, (**c**) close-up view of SEM image of sample B1 overlaid with illite and kaolinite distribution, (**d**) SEM image of sample B2 overlaid with illite and kaolinite distribution, (**e**) overall mineral composition distribution of sample B1, (**f**) close-up view of SEM image of sample B1 overlaid with illite and kaolinite distribution. The yellow dashed area is used for enlargement and then displayed on the right side.

As shown in Figure 3a, the larger gravel particles in sample B1 are embedded within a significant amount of detrital matrix. Some regions of the matrix are well-compacted, while numerous intergranular pores are developed among other detrital particles. Figure 3b indicates that the gravel particles in sample B1 are composed of quartz and feldspar, whereas the detrital matrix consists of a mixture of quartz and feldspar. The feldspar-dominated gravels contain a combination of K-feldspar and albite, and some quartz gravel particles also incorporate minor amounts of feldspar. The fillings within the detrital matrix are primarily calcite. Clay minerals (illite and kaolinite) are predominantly distributed along the edges of the detrital particles within the matrix, as illustrated in Figure 3c. Sample B2 exhibits generally similar characteristics. Although the development of intergranular pores in sample B2 is less pronounced than in B1 (Figure 3d), its gravel particles and detrital matrix are compositionally consistent with those of B1, as shown in Figure 3e. Compared to B1, the matrix fillings in B2 contain more siderite and less calcite. The distribution of clay

minerals is largely consistent with that in B1, also occurring within the matrix and along the boundaries between gravel particles and matrix detritus, as depicted in Figure 3f.

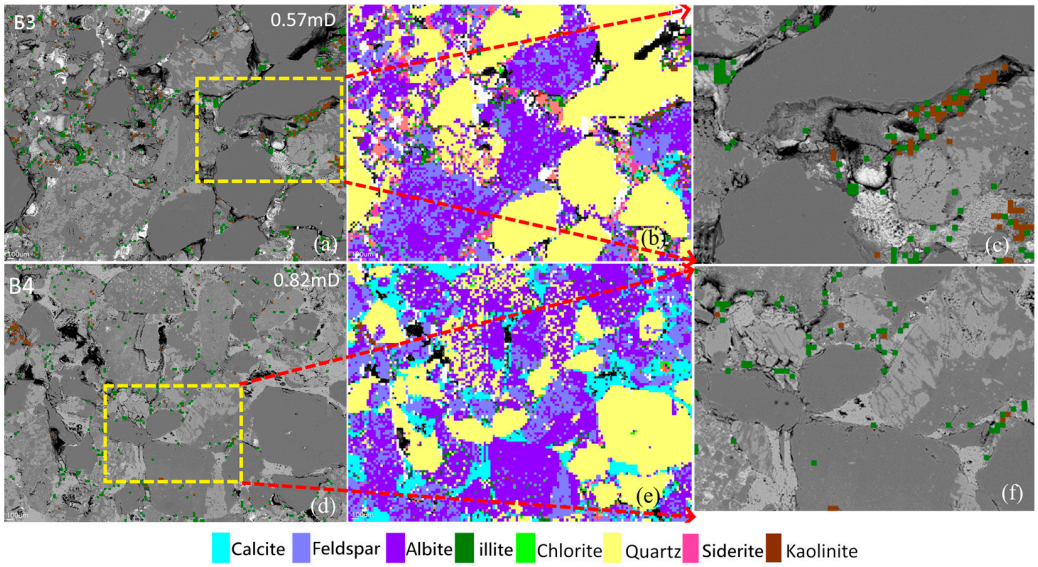


Figure 4. Surface morphology and mineral composition distribution of samples B3 and B4. (**a**) SEM image of sample B3 overlaid with illite and kaolinite distribution, (**b**) overall mineral composition distribution of sample B3, (**c**) close-up view of SEM image of sample B3 overlaid with illite and kaolinite distribution, (**d**) SEM image of sample B4 overlaid with illite and kaolinite distribution, (**e**) overall mineral composition distribution of sample B4, (**f**) close-up view of SEM image of sample B4 overlaid with illite and kaolinite distribution. The yellow dashed area is used for enlargement and then displayed on the right side.

As shown in Figure 4a,d, compared with samples B1 and B2, samples B3 and B4 exhibit lower detrital content within the inter-gravel matrix and a higher degree of cementation, resulting in correspondingly lower permeability than B1 and B2. According to the mineral composition distribution results in Figure 4b,e, the gravel composition of samples B3 and B4 is consistent with that of B1 and B2. In the inter-gravel matrix, sample B3 is primarily composed of feldspar, calcite, and siderite, while sample B4 consists mainly of calcite and feldspar. As shown in Figure 4c,f, similar to B1 and B2, clay minerals are predominantly distributed along the edges of gravel particles and within the inter-gravel matrix.

Gravels constitute the majority of the rock mass and volume, yet they contribute very little to seepage pathways, except for limited trans-gravel fractures and rare dissolution pores within gravel particles [22]. The pore structure and seepage capacity of the remaining inter-gravel matrix largely determine the overall fluid flow capability of the core [23]. RoqSCAN results indicate that although the total clay mineral content in the four samples with different permeabilities is below 5%, when considering the inter-gravel matrix alone, the proportion of clay minerals increases significantly. These clay minerals are almost entirely located within the inter-gravel matrix or along the boundaries between matrix detritus and gravels—precisely the regions that form critical seepage channels in the conglomerate, particularly fractures along gravel edges. Therefore, the expansion or migration of these clay minerals can substantially influence the overall seepage capacity of the sample.

Although the detected clay minerals do not include montmorillonite, which exhibits the strongest water sensitivity, illite still possesses water-swelling characteristics, and kaolinite is a typical velocity-sensitive clay mineral prone to detachment and subsequent blockage of seepage channels under certain flow conditions. The pore structure of the conglomerates in the study area, combined with the concentration of clay minerals at

gravel edges, may exacerbate the velocity sensitivity of the samples. Thus, the pronounced sensitivity observed under low clay mineral content in the study area results from the combined effects of water and velocity sensitivity, influenced by pore structure, clay mineral content, and distribution characteristics.

3.3. Pore Structure Variation

The original raw files obtained from CT scanning were 16-bit gray-scale 3D Raw files with a voxel resolution of 3400 × 3400 × 2600, and the size of the Raw file is approximately 60 GB for each sample. Directly processing the original files resulted in extremely low computational efficiency, and the VRAM required for calculating the PNM network exceeded the total VRAM of the hardware platform. To increase data processing efficiency and successfully calculate the PNM, as shown in Figure 5, we extracted sub-volumes (the yellow dashed line part) from the central part of the samples. The size of the sub-volume is around 2.5GB. It can be seen that the CT scan results of the three samples with different permeability are similar to the SEM scan results. The low-permeability sample C1 (1.96 mD) has higher cementation of inter-gravel matrix, with only a small amount of intergranular fractures observable on the surface (as shown in Figure 5a). In contrast, the higher permeability samples C2 (11.22 mD) and C3 (59.5 mD) show certain intergranular pores on the surface (as shown in Figure 5b,c).

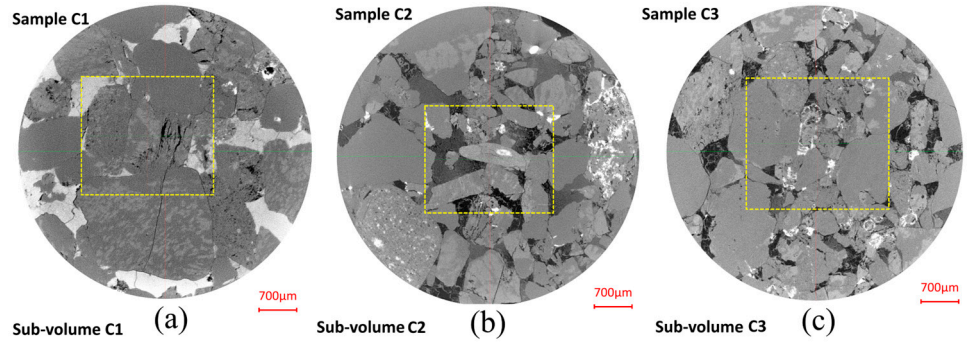


Figure 5. Section of the full-scale sample and the sub-volumes for pore extraction and PNM computation, and its 3D rendering result. (**a**) section of sample C1, (**b**) section of sample C2, (**c**) section of sample C3. The yellow dashed area represents the selected sub-volume region.

3.3.1. Two-Dimensional Slice Analysis of Pore Structure Variation

We selected specific slices from the three samples where pore changes before and after water flooding were noticeable as examples to analyze the specific pore changes. The example slice for sample C1 is shown in Figure 6.

Figure 6 shows the 375th slice along the z-axis from the sample C1 dataset, which comprises a total of 650 slices in the Z-direction. Figure 6a displays pore structures before water flooding, and Figure 6b shows the same region after water flooding. Sample C1, with a permeability of 1.96 mD, has the lowest permeability among the three samples. The slice reveals that pore types are primarily intergranular micro-fractures, intergranular matrix pores, and a limited number of intragranular dissolution pores. Locations with significant changes after water flooding are highlighted with yellow and red dashed lines. Positions 1 and 2, which contained well-developed gravel-edge fractures before flooding, exhibited almost complete fracture closure after water flooding. At Position 3, intergranular pores were present before water flooding, with debris visible at the arrow-marked location. After flooding, the debris had disappeared, indicating particle migration. Fracture closure and particle migration are two key mechanisms contributing to permeability sensitivity. Notably, not all porous regions were affected by water flooding. For example, the gravel-edge

fracture in the lower-right section of the slice showed no significant change in morphology or aperture. The areal porosity of the C1 sample slice decreased from 4.376% before flooding to 3.686% afterward.

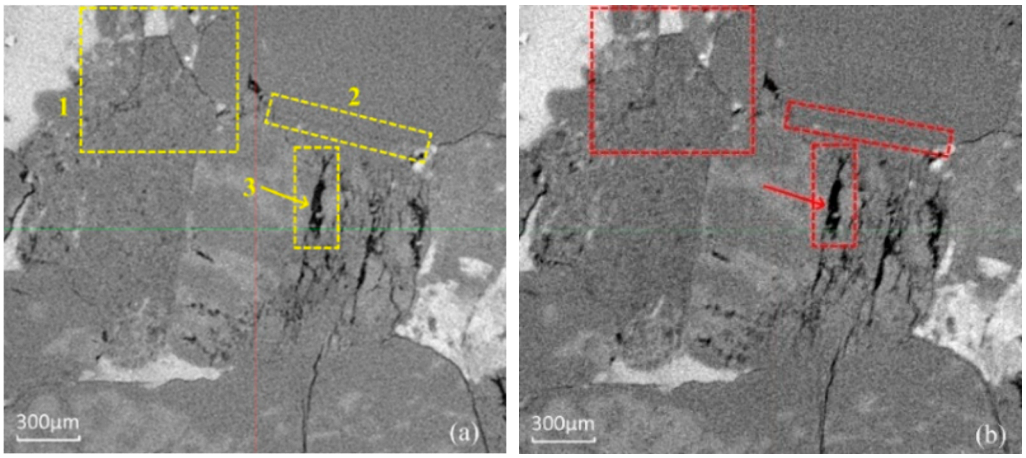


Figure 6. Representative cross-sections of pore structure in sample C1, (**a**) before and (**b**) after water flooding (z-axis position: 375). The yellow and red dashed areas represent the comparison regions for the variation of cracks.

Figure 7 displays a representative slice (the 611th slice along the z-axis) from the sample C2 dataset. With a permeability of 11.22 mD, sample C2 exhibits a greater abundance of matrix pores and intergranular pores compared to sample C1, along with observable intraparticle pores. The areal porosity of the C2 slice was 14.551% before flooding and 14.127% after flooding. Additionally, the gravel particles in sample C2 are smaller than those in C1. Significant changes in pore structure can be observed in the slice. As indicated by position 1 in Figure 7a, an intraparticle fracture connected to the intergranular matrix below shows reduced connectivity on the right side after water flooding. Fracture apertures at positions 2–6 clearly contracted but did not completely close, unlike what was observed in sample C1. In contrast, the intergranular pore at position 8 in the upper-right region, the matrix-supported intergranular fracture at position 9, and the intergranular pore at position 10 remained largely unaffected.

Figure 8 displays the 594th slice along the z-axis of the sample C3 data volume. Compared to samples C1 and C2, C3 exhibits a higher proportion of intergranular pores. The areal porosity was 17.9% before water flooding and 17.7% afterward. Apart from the closure of the intergranular fracture within the yellow frame at Position 1, only minor changes were observed in the intergranular fractures, intergranular pores, and intragranular pores at Positions 2 to 4.

From these slice examples, it can be concluded that samples across the three permeability ranges all undergo certain structural alterations after water flooding. These are manifested as the narrowing or closure of intergranular fractures, the reduction in aperture of dissolution pores within the matrix, and the migration of debris inside some pores. It is noteworthy, however, that even in low-permeability samples, some pores remain largely unaffected by the flooding process.

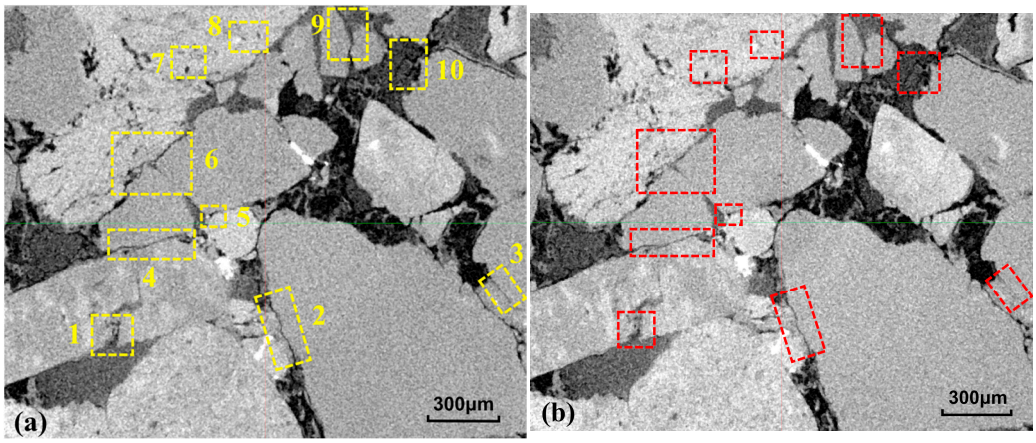


Figure 7. Representative cross-sections of pore structure in sample C2, (**a**) before and (**b**) after water flooding (z-axis position: 611). The yellow and red dashed areas represent the comparison regions for the variation of cracks.

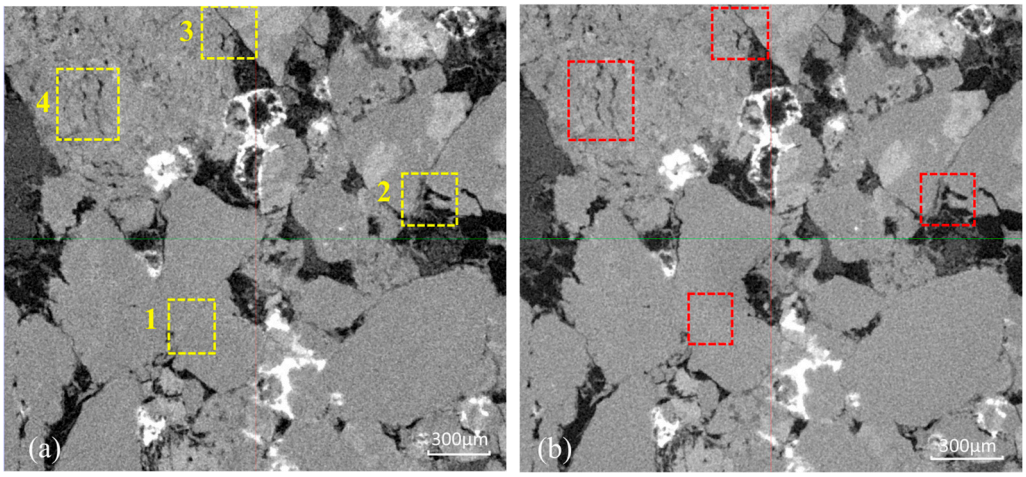


Figure 8. Representative cross-sections of pore structure in sample C3, (**a**) before and (**b**) after water flooding (z-axis position: 594). The yellow and red dashed areas represent the comparison regions for the variation of cracks.

3.3.2. Statistical Analysis of Pore Structure Network

Using 2D slice samples, specific instances of pore structure alterations in the three samples were analyzed before and after water flooding, clarifying the types of pore changes that occurred. However, to assess how the overall pore parameters of the core evolve, further statistical analysis integrated with PNM is required. The specific results are presented in Figure 9, with pore and throat sizes represented by color mapping.

Comparison of the PNM before and after water flooding reveals that in sample C1, large sections of the pore network closed or disappeared after flooding (as indicated by the red dashed box in Figure 9a,d. The overall pore network also became sparser, indicating a significant reduction in the total number of pores. In sample C2, partial closure occurred in the local pore network on the left side (within the red dashed box in Figure 9b,e, and the number of pores decreased moderately in certain regions after flooding. In contrast, sample C3 exhibited no significant pore closure or disappearance after water flooding.

It is worth noting that in sample C1, local enhancements in network connectivity and an increased number of pores were observed in the lower-right region, as marked by the light blue dashed box in Figure 9a. Additionally, in areas originally characterized by clustered pores and strong connectivity, some pores exhibited enlarged apertures after flooding, manifested as expanded yellow and red regions in the central pore network.

However, such changes were not observed in sample C2. The pore distribution in sample C2 was more homogeneous compared to C1, and the overall connectivity of the pore network was better. Instead, a more general reduction in pore throat sizes was observed across the network after flooding, reflected by a noticeable decrease in yellow and red regions. In sample C3, the overall extent and structure of the pore network remained largely unchanged. Nevertheless, a trend of pore enlargement was still discernible, particularly in regions that originally consisted of larger pores. This was evidenced by the significant expansion of yellow and red regions in the pore network after flooding (as shown in Figure 9c,f).

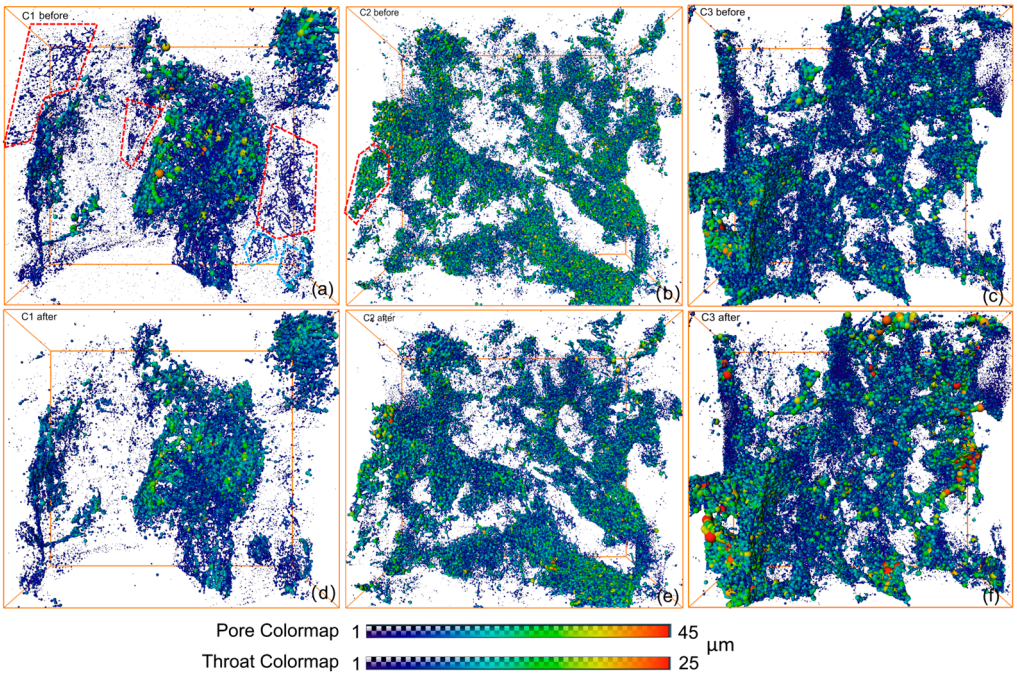


Figure 9. PNM networks of the samples before and after water flooding. (**a**) sample C1 before flooding, (**b**) sample C2 before flooding, (**c**) sample C3 before flooding, (**d**) sample C1 after flooding, (**e**) sample C2 after flooding, (**f**) sample C3 after flooding. The red dashed areas represent the regions for the variation of pore network.

These changes in PNM suggest that damage to the pore structure during water flooding may be more pronounced in non-main flow channels. In major flow pathways, in contrast, scouring by fluids and the dislodgment of particles may lead to localized enlargement, especially in regions subjected to sustained fluid flow. In sample C2, which exhibits a relatively uniform pore network, pore enlargement due to high-permeability channel flushing is less evident. Instead, the dominant trend is a contraction in pore scales across the network.

To further refine the changes in pore network parameters of the three samples before and after water flooding, the pore size, throat size, coordination number, and throat length of the PNM networks were statistically analyzed. The results of sample C1 are shown in Figure 10.

As shown in Figure 10a, the total number of pores in sample C1 decreased significantly after water flooding. Pores smaller than 7 μm showed a notable reduction, especially those under 2 μm, which decreased by more than 50%. In contrast, the number of pores larger than 7 μm increased slightly, though the overall growth was limited. As illustrated in Figure 10b, the number of throat diameters larger than 3 μm decreased markedly after water flooding, while throats smaller than 3 μm exhibited a slight increase in count. Regarding

throat length, as shown in Figure 10c, the overall trend post-flooding showed a decline in the number of throats with lengths between 13 and 47 μm, with a particularly significant reduction in those measuring 18–33 μm. In comparison, shorter throats (<8 μm) and longer throats (>48 μm) increased in number. Notably, throats longer than 56 μm more than doubled, though they account for a very small proportion of the total throat population. In terms of coordination number, as shown in Figure 10d, the number of pores with coordination numbers below 4 decreased significantly, with a reduction of over 50% for pores having coordination numbers under 2. Pores with coordination numbers above 6 experienced a modest increase.

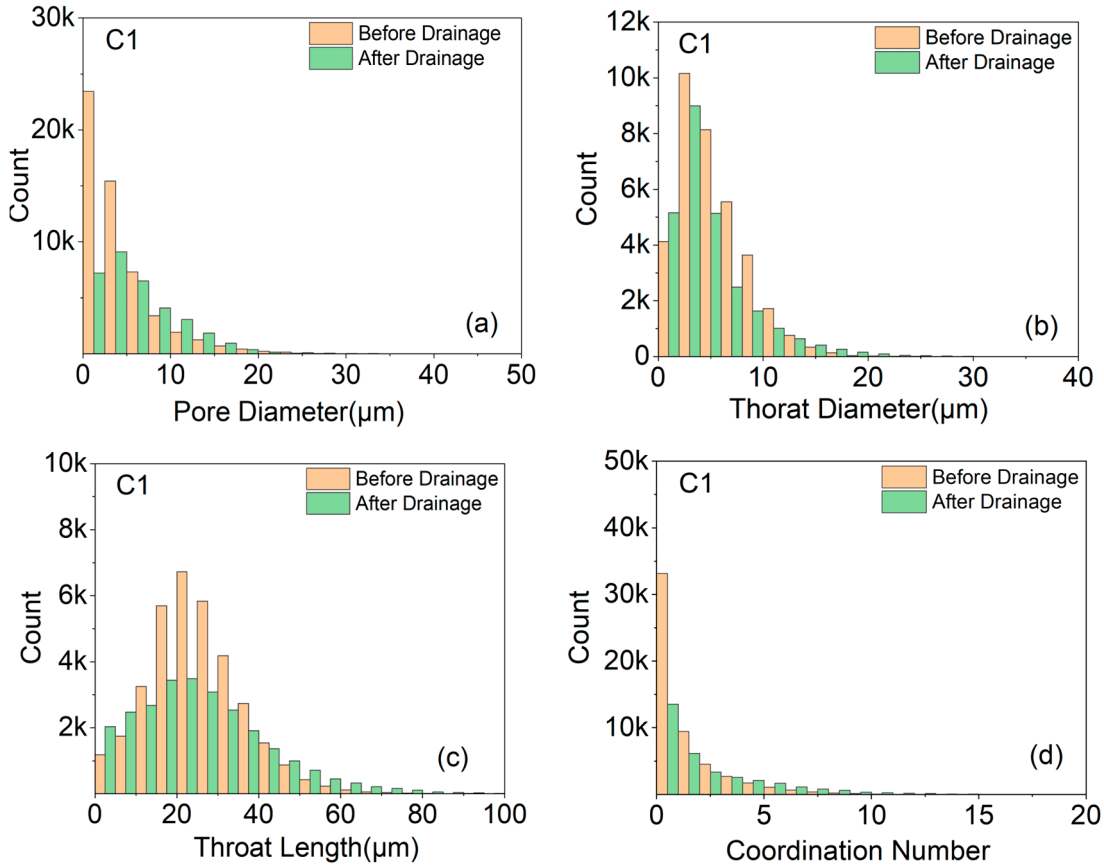


Figure 10. Changes in pore amount with different pore sizes, throat diameters, coordination numbers, and throat lengths in sample C1 before and after water flooding. (**a**) The pore diameter variation before and after drainage; (**b**) The throat diameter variation before and after drainage; (**c**) The throat length variation before and after drainage; (**d**) The coordination number variation before and after drainage.

Based on the relationship between permeability and sensitivity discussed in the previous section, sample C2 is classified as a moderately water-sensitive sample. As shown in Figure 11a, the total number of pores and throats in sample C2 is significantly higher than that in sample C1. In addition, the throat length and average coordination number of sample C2 are considerably better than those of C1. Nevertheless, the overall variation in pore network parameters after water flooding is generally similar between samples C2 and C1. In terms of the total number of pores across different scales, Figure 11a shows that after water flooding, both samples exhibit a substantial decrease in the number of small pores. Specifically, the total number of pores smaller than 7 μm decreased markedly in sample C1, while the reduction in sample C2 was more pronounced for pores below 10 μm. In contrast, a slight increase was observed in the number of pores larger than 10 μm.

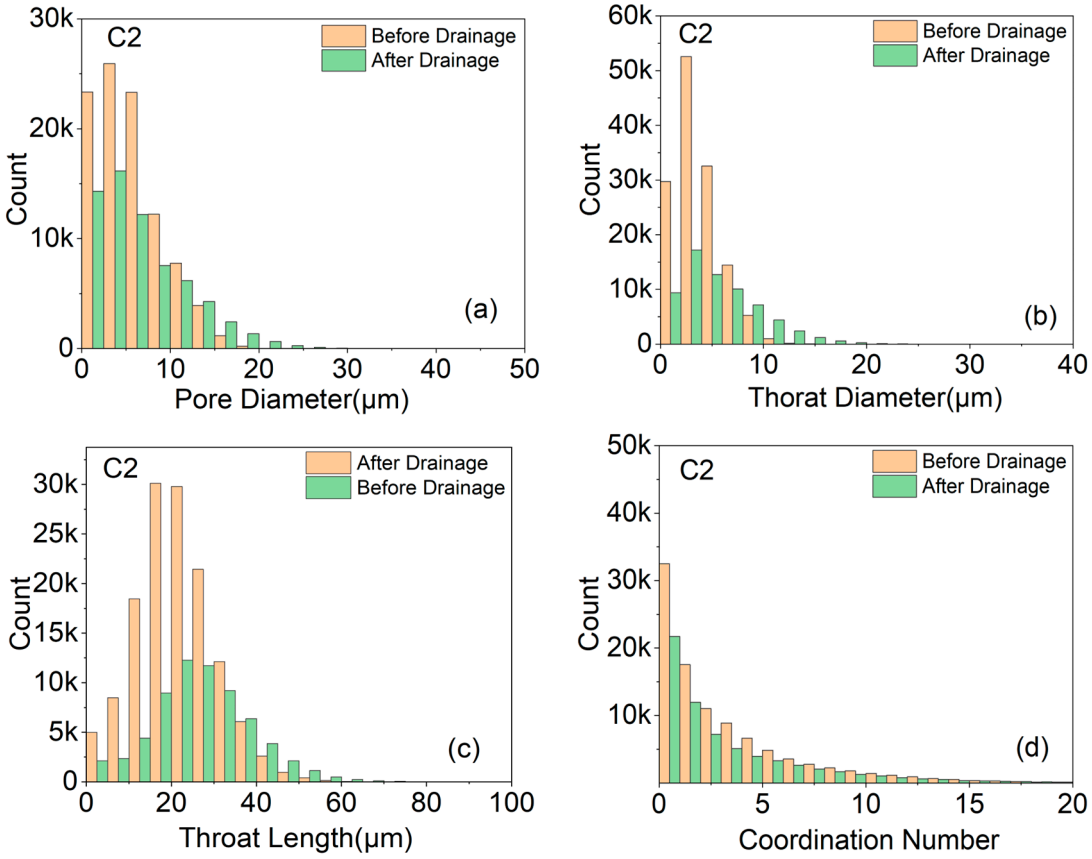


Figure 11. Changes in pore amount with different pore sizes, throat diameters, coordination numbers, and throat lengths in sample C2 before and after water flooding. (**a**) The pore diameter variation before and after drainage; (**b**) The throat diameter variation before and after drainage; (**c**) The throat length variation before and after drainage; (**d**) The coordination number variation before and after drainage.

Regarding throat size changes, as shown in Figure 11b, sample C2 exhibited a significant decrease in the number of throats smaller than 7 μm after flooding, with those around 4 μm decreasing by more than 50%. Conversely, the number of throats larger than 7 μm showed a noticeable increase. Furthermore, the maximum throat size in sample C2 increased from approximately 13 μm before flooding to about 20 μm after flooding. In terms of throat length variation, as shown in Figure 11c, the changes before and after flooding were also pronounced in sample C2 compared to C1. The variation in C2 was bounded around 40 μm: the number of throats shorter than 40 μm decreased significantly, while those longer than 40 μm increased to some extent. As for the coordination number, as shown in Figure 11d, almost all pores across different coordination values experienced a certain degree of reduction after flooding. Pores with coordination numbers below 5 decreased relatively significantly, while those with coordination numbers above 5 underwent only minor changes.

For the weakly water-sensitive sample C3, changes in pore size, throat size, throat length, and coordination number were still observed before and after water flooding, as detailed in Figure 12. The variation trends are entirely distinct from those of the strongly and moderately water-sensitive samples. After flooding, the weakly water-sensitive sample exhibited an increasing trend in the number of pores below 10 μm, while the quantity of pores larger than 10 μm remained almost unchanged (Figure 12a). In terms of throat characteristics, as shown in Figure 12b, the number of throats smaller than 5 μm and larger than 15 μm increased after water flooding, whereas throats within the 5–10 μm range

showed a slight decrease. Regarding throat length, as shown in Figure 12c, the number of throats shorter than 15 μm and longer than 40 μm increased, while a relatively noticeable reduction occurred in throats with lengths between 15 μm and 40 μm.

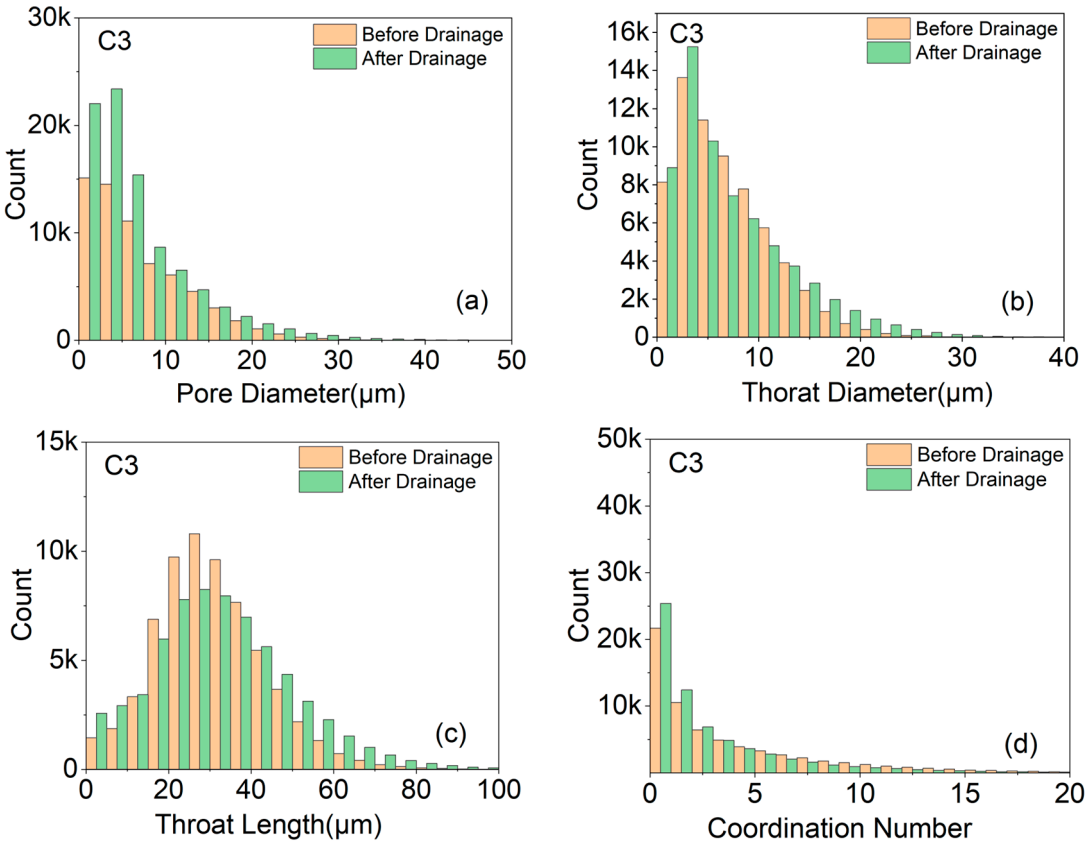


Figure 12. Changes in pore amount with different pore sizes, throat diameters, coordination numbers, and throat lengths in sample C3 before and after water flooding. (**a**) The pore diameter variation before and after drainage; (**b**) The throat diameter variation before and after drainage; (**c**) The throat length variation before and after drainage; (**d**) The coordination number variation before and after drainage.

As for the coordination number, as shown in Figure 12d, a slight increase was observed in the number of throats with coordination numbers below 3 after water flooding. In contrast, the overall number of pores with coordination numbers above 3 underwent negligible change.

4. Discussion

In this study, we reveal a fundamental inverse correlation between the initial gas-measured permeability and the degree of permeability damage following water flooding in the Mahu conglomerate reservoir. Samples with lower initial permeability consistently suffered more severe impairment. This finding underscores that lithological heterogeneity is a primary control on water sensitivity, where even modest amounts of sensitive clay minerals can induce disproportionate damage in low-permeability rocks.

The underlying mechanism for this inverse correlation is intrinsically linked to the distinct pore structure characteristics of different permeability classes. Our integrated SEM and micro-CT analyses indicate that the pore networks are dominated by gravel-edge fractures and intergranular pores within the fine-grained matrix. The gravel components themselves contribute minimally to the fluid flow pathways. In low-permeability samples, the inter-gravel matrix is more heavily cemented, and the pore system relies critically

on a limited number of narrow, poorly connected gravel-edge fractures. These restricted channels possess low coordination numbers, meaning they have few alternative pathways. When subjected to processes such as clay swelling or the mobilization of detached particles, these critical throats are highly susceptible to complete blockage. This phenomenon was quantitatively confirmed through PNM of a low-permeability sample C1, which demonstrated that at least two discrete regions of gravel-edge fractures lost all flow capacity after water flooding.

Conversely, high-permeability samples possess a more robust and redundant pore network. This network comprises not only fracture pathways but also a well-developed system of intergranular pores with larger apertures and higher coordination numbers. The abundance of interconnected flow channels ensures that the effects of localized clogging, due to clay swelling or particle migration in a single throat, are mitigated. The overall connectivity remains largely intact, as evidenced by the PNM results of samples C2 and C3, where no entire pore network region was completely disconnected despite some localized damage.

Another critical finding of this work is the significant permeability damage observed despite a low bulk clay mineral content. This apparent contradiction is resolved by considering the unique pore structure of the conglomerate and the specific distribution of clay minerals. Conventional whole-rock XRD analysis does not distinguish between the inert gravel particles and the reactive inter-gravel matrix. Since the gravels contribute negligibly to fluid flow, the clay minerals that actually govern permeability damage are those coating the gravel surfaces and residing within the pore spaces of the matrix. Data from RoqSCAN indicate that the clay minerals (predominantly illite and kaolinite) are precisely concentrated in these strategic locations: on gravel surfaces (including fracture surfaces along gravel edges) and within the inter-gravel matrix. After excluding the volume occupied by the gravels, the relative content of clay minerals in these critical flow zones is considerably higher than the bulk measurement suggests.

The types of clay minerals present further exacerbate the water sensitivity. Illite exhibits certain swelling properties; although its expansion rate is lower than montmorillonite, it can generate significant swelling stress rapidly [24]. Kaolinite, a typical migratory clay, is prone to detachment and subsequent migration, leading to pore throat blockage [25]. The co-occurrence of these two minerals, concentrated in the key flow channels like gravel-edge fractures and the matrix, creates a coupled damaging mechanism. This explains the strong water sensitivity observed in the study area, even where bulk clay content is low.

The impact of water flooding is not a simple uniform reduction in all pore and throat dimensions. In high-permeability samples, the flooding process appeared to cause the swelling and contraction of long throats and the detachment of particles within some larger pores. This detachment paradoxically led to an increase in the number of large pores and throats post-flooding. However, the subsequent migration and lodging of these dislodged particles caused a reduction in medium-length throats. CT results suggest that these long throats are often wide-aperture, extended gravel-edge fractures that act as primary conduits; fluid scouring during flooding may further widen and extend them.

The response differed markedly in more water-sensitive samples. In strongly water-sensitive samples, flooding had a more pronounced effect on reducing the average pore size, shortening the effective throat length, and decreasing the overall coordination number of the network. In contrast, moderately water-sensitive samples exhibited a significant reduction in the total number of pores (especially small pores) and throats (particularly small throats), alongside a marked decline in coordination number. However, these samples did not experience widespread throat disconnection and thus did not show a net increase in short throats.

It must be clarified that the water sensitivity mechanisms we have revealed do not apply to all conglomerates in the Xinjiang Mahu area. Our findings regarding the mechanisms and their impact on pore structure are specifically valid for cases where the gravels themselves are clay-free, and the limited clay minerals are primarily distributed in the inter-gravel matrix and gravel-edge fractures. There are substantial conglomerate reservoirs, particularly those with gravel components composed of tuff clasts and mudstone clasts, which strongly conform to the pattern where higher clay mineral content corresponds to intensified water sensitivity [26,27]. In these conglomerates, clay mineral content may occupy up to 72.7% of the gravel composition [13]. For such reservoirs, during seepage processes, the contact between gravel and fluids induces swelling and dispersion of clay minerals within the gravel, thereby destroying the supportive skeletal framework formed between gravel particles, and consequently severely impairing reservoir permeability. For these conglomerates, the clay minerals in the matrix contribute minimally to overall reservoir damage. Some researchers contend that the clay minerals within these gravel particles represent the primary mineralogical factor hindering efficient development of conglomerate oil reservoirs in the Mahu area [5,8].

Finally, it is important to acknowledge the methodological limitations of this study. The micro-CT characterization, while powerful, is constrained by a resolution limit of 1.896 μm. Consequently, pores and throats smaller than this threshold could not be reliably identified or their evolution tracked. Furthermore, the selection of grayscale thresholds for pore identification, despite using in situ scanning and grayscale normalization to improve consistency, remains a source of potential deviation in the precise size and location of segmented pores. Image preprocessing techniques for noise reduction, while necessary for segmentation, inherently alter the original data. Emerging machine learning-based segmentation methods offer promise but have not yet fully overcome these challenges, indicating a need for continued technological advancement for more precise and higher-resolution pore-scale analysis.

5. Conclusions

Based on the findings of this study, the following conclusions are drawn regarding some of the tight conglomerate reservoirs in the Mahu Sag:

(1) A significant inverse correlation exists between the degree of water sensitivity damage and initial gas permeability, suggesting that formations with lower initial permeability undergo more severe impairment due to water sensitivity.

(2) The notable water sensitivity observed in these low-clay conglomerate formations stems from the combined effect of water and velocity sensitivity, mainly caused by illite and kaolinite concentrated in critical flow channels such as gravel-edge fractures and the matrix.

(3) Water sensitivity does not degrade all pore structure parameters uniformly; it can result in localized enlargement of certain macropores and throats, reflecting heterogeneous changes in pore geometry.

(4) The structural response to water sensitivity varies with permeability: medium–low permeability samples with limited flow pathways show clear damage from clay swelling and particle migration, while high-permeability samples with well-connected pore networks exhibit strong resistance to overall damage and may even experience enhancement of major flow paths through fluid flushing.

(5) Water sensitivity predominantly deteriorates pore parameters in smaller pores, while potentially enhancing those in larger pores. The critical pore-size threshold distinguishing macro- and micro-pores exhibits an inverse relationship with permeability, manifesting as reduced threshold values in lower-permeability formations.

Author Contributions: Conceptualization, D.L. and K.C.; methodology, D.L.; software, D.L. and E.S.; validation, D.L.; formal analysis, K.C. and E.S.; investigation, D.L., K.C. and E.S.; resources, D.L.; data curation, D.L. and E.S.; writing—original draft preparation, D.L. and K.C.; writing—review and editing, D.L. and K.C.; visualization, D.L. and K.C.; supervision, D.L.; project administration, D.L.; funding acquisition, D.L. All authors have read and agreed to the published version of the manuscript.

Funding: This research was funded by the Research Foundation of China University of Petroleum-Beijing at Karamay, grant number XQZX20230011. Natural Science Foundation of Xinjiang Uygur Autonomous Region. Region, grant number 2022D01B144; Youth Doctoral Project of the Tianchi Talent Introduction Program.

Institutional Review Board Statement: Not applicable.

Informed Consent Statement: Not applicable.

Data Availability Statement: The raw data supporting the conclusions of this article will be made available by the authors on request.

Conflicts of Interest: Author Erhan Shi was employed by the company PetroChina Southwest Oil & Gas Field Company. The remaining authors declare that the research was conducted in the absence of any commercial or financial relationships that could be construed as a potential conflict of interest.

References

1. He, Y.C.; Zhang, C.R. The world's largest conglomerate oil field discovered in Junggar Basin, Xinjiang. *Geol. China* **2017**, *44*, 1174.
2. Xiao, M.; Wu, S.; Yuan, X.; Cao, Z.; Xie, Z. Diagenesis effects on the conglomerate reservoir quality of the Baikouquan Formation. Junggar Basin, China. *J. Pet. Sci. Eng.* **2020**, *195*, 107599. [CrossRef]
3. Jia, H.; Ji, H.; Wang, L.; Gao, Y.; Li, X.; Zhou, H. Reservoir quality variations within a conglomeratic fan-delta system in the Mahu sag. northwestern Junggar Basin: Characteristics and controlling factors. *J. Pet. Sci. Eng.* **2017**, *152*, 165–181. [CrossRef]
4. He, J.; Tang, H.; Wang, L.; Yang, Z.; Wang, Y.; Zhang, X.; Hu, Q.; Wan, B. Genesis of heterogeneity in conglomerate reservoirs: Insights from the Baikouquan formation of Mahu sag. in the Junggar Basin, China. *Pet. Sci. Technol.* **2021**, *39*, 11–29. [CrossRef]
5. Yu, Z.; Wang, Z.; Adenutsi, C.D. Genesis of authigenic clay minerals and their impacts on reservoir quality in tight conglomerate reservoirs of the Triassic Baikouquan formation in the Mahu Sag, Junggar Basin, Western China. *Mar. Pet. Geol.* **2023**, *148*, 106041. [CrossRef]
6. Li, J.; Zhang, K.; Cheng, N.; Xing, Z.; Wang, S.; Wang, B.; Liang, T. Optimization and evaluation of stabilizers for tight water-sensitive conglomerate reservoirs. *ACS Omega* **2022**, *7*, 5921–5928. [CrossRef]
7. Jin, L.; Liu, Y.; Gao, J.; Hao, Z. Quantitative Interpretation of Water Sensitivity Based on Well Log Data: A Case of a Conglomerate Reservoir in the Karamay Oil Field. *Lithosphere* **2021**, *2021*, 5992165. [CrossRef]
8. Du, S.; Zhao, A.; Zhou, W.; Wei, Y. Elemental and mineralogical mechanisms controlling the storage and flow performances of tight conglomerates. *Int. J. Hydrogen Energy* **2024**, *65*, 479–495. [CrossRef]
9. Zhang, L.; Zhou, F.; Zhang, S.; Wang, Y.; Wang, J.; Wang, J. Investigation of water-sensitivity damage for tight low-permeability sandstone reservoirs. *ACS Omega* **2019**, *4*, 11197–11204. [CrossRef] [PubMed]
10. Wang, L.; Zhang, H.; Peng, X.; Wang, P.; Zhao, N.; Chu, S.; Wang, X.; Kong, L. Water-sensitive damage mechanism and the injection water source optimization of low permeability sandy conglomerate reservoirs. *Pet. Explor. Dev.* **2019**, *46*, 1218–1230. [CrossRef]
11. Liu, C.; Yin, C.; Lu, J.; Sun, L.; Wang, Y.; Hu, B.; Li, J. Pore structure and physical properties of sandy conglomerate reservoirs in the Xujiaweizi depression, northern Songliao Basin, China. *J. Pet. Sci. Eng.* **2020**, *192*, 107217. [CrossRef]
12. Zhou, Y.; Wu, S.; Li, Z.; Zhu, R.; Xie, S.; Jing, C.; Lei, L. Multifractal study of three-dimensional pore structure of sand-conglomerate reservoir based on CT images. *Energy Fuels* **2018**, *32*, 4797–4807. [CrossRef]
13. Du, S.; Zhao, A.; Wei, Y. The dominant mineralogical triggers hindering the efficient development of the world's largest conglomerate oilfield. *Int. J. Hydrogen Energy* **2024**, *60*, 688–701. [CrossRef]
14. Ye, Y.; Jiang, Q.; Liang, C.; Xiong, Q.; Qiu, Z.; Li, S.; Zhang, H. Experimental study on the mechanism of water-sensitive injury in Upper Urho Formation sand and gravels of the Mahu well area. *Sci. Technol. Eng.* **2022**, *22*, 11895–11903.
15. Song, Y.L.; Song, Z.J.; Zhang, Y.F.; Xie, Z.H.; Zhang, L.C.; Wang, D.G.; Hui, G. Pore scale performance evaluation and impact factors in nitrogen huff-n-puff EOR for tight oil. *Pet. Sci.* **2022**, *19*, 2932–2940. [CrossRef]
16. Zhu, Q.; Wu, K.; Guo, S.; Peng, F.; Zhang, S.; Jiang, L.; Li, J.; Feng, D.; Zhang, Y.; Chen, Z. Pore-scale investigation of CO_2-oil miscible flooding in tight reservoir. *Appl. Energy* **2024**, *368*, 123439. [CrossRef]

17. Liu, Z.; Li, Y.; Luan, H.; Gao, W.; Guo, Y.; Chen, Y. Pore scale and macroscopic visual displacement of oil-in-water emulsions for enhanced oil recovery. *Chem. Eng. Sci.* **2019**, *197*, 404–414. [CrossRef]
18. Liu, D.; Zhao, Z.; Cai, Y.; Sun, F.; Zhou, Y. Review on applications of X-ray computed tomography for coal characterization: Recent progress and perspectives. *Energy Fuels* **2022**, *36*, 6659–6674. [CrossRef]
19. Ju, Y.; Xi, C.; Zhang, Y.; Mao, L.; Gao, F.; Xie, H. Laboratory in situ CT observation of the evolution of 3D fracture networks in coal subjected to confining pressures and axial compressive loads: A novel approach. *Rock Mech. Rock Eng.* **2018**, *51*, 3361–3375. [CrossRef]
20. *SY/T 5358-2010*; Oil and Natural Gas Industry Standard of the People's Republic of China—Formation Damage Evaluation by Flow Test. China National Energy Administration: Beijing, China, 2010.
21. *SY/T 5163–2018*; Analysis Method for Clay Minerals and Ordinary Non-Clay Minerals in Sedimentary Rocks by the X-ray Diffraction. China National Energy Administration: Beijing, China, 2018.
22. Liu, Z.; Li, S.; Zhang, J.; Li, W.; Li, M.; Xu, Q. Quantitative Study of Diagenesis and Dissolution Porosity in Conglomerate Reservoirs. *Chem. Technol. Fuels Oils* **2023**, *58*, 1035–1045. [CrossRef]
23. Tian, W.; Lu, S.; Huang, W.; Wang, W.; Li, J.; Gao, Y.; Zhan, Z.; Sun, Y. Quantifying the control of pore types on fluid mobility in low-permeability conglomerates by integrating various experiments. *Fuel* **2020**, *275*, 117835. [CrossRef]
24. Zhang, J.; Peng, Y.; Wang, C.; Zhang, W.; Luo, X. Interlayer water absorption expansion and surface hydration properties of montmorillonite and kaolinite. *Miner. Eng.* **2025**, *234*, 109713. [CrossRef]
25. Wang, B.; Qin, Y.; Shen, J.; Wang, G.; Zhang, Q. Influence of stress and formation water properties on velocity sensitivity of lignite reservoir using simulation experiment. *Fuel* **2018**, *224*, 579–590. [CrossRef]
26. Ye, Y.; Xiao, Y.; Kou, G. Water-sensitive effect and main controlling factors of Baikouquan Formation reservoir in Mahu Sag, Junggar Basin, China. *J. Chengdu Univ. Technol. (Sci. Technol. Ed.)* **2022**, *49*, 729–738.
27. Zhao, A.; Du, S. Hydration-induced damage of tight conglomerates. *Chem. Eng. J.* **2024**, *495*, 153426. [CrossRef]

Disclaimer/Publisher's Note: The statements, opinions and data contained in all publications are solely those of the individual author(s) and contributor(s) and not of MDPI and/or the editor(s). MDPI and/or the editor(s) disclaim responsibility for any injury to people or property resulting from any ideas, methods, instructions or products referred to in the content.